Letter

In-plane epitaxy-strain-tuning intralayer and interlayer magnetic coupling in $CrSe_2$ and $CrTe_2$ monolayers and bilayers

Linlu Wu,[*] Linwei Zhou,[*] Xieyu Zhou, Cong Wang,[†] and Wei Ji[‡]

Beijing Key Laboratory of Optoelectronic Functional Materials & Micro-Nano Devices, Department of Physics, Renmin University of China, Beijing 100872, People's Republic Of China

(Received 10 March 2022; revised 16 July 2022; accepted 18 July 2022; published 1 August 2022)

Mismatched lattice constants at a van der Waals epitaxy interface often introduce in-plane strains to the lattice of the epitaxial layer, termed epitaxy strain, wherein the strains do not follow the intralayer Poisson's relation. In this study, we obtained the magnetic phase diagrams of $CrSe_2$ and $CrTe_2$ mono- and bilayers under epitaxy strain up to 8%, as predicted using density functional theory calculations. The magnetic phase diagrams indicate that the in-plane epitaxy strain manipulates either the intra- or interlayer magnetism. The in-plane strain varies the interlayer distance, defined using an interlayer Poisson's ratio, which determines whether the interlayer magnetism follows a Bethe–Slater curve-like (BSC-like) or a reversed BSC-like behavior, depending on the in-plane magnetism. The tunability of the intralayer magnetism is a result of competing intralayer Cr–Cr superexchange interactions. A graphene substrate was introduced to examine the validity of our diagrams in practice. This study also afforded a tentative explanation on the previously reported magnetizations in $CrSe_2$ and $CrTe_2$ epitaxial mono- or bilayers under epitaxy strains, which had given rise to some controversy.

DOI: 10.1103/PhysRevB.106.L081401

Magnetism in two-dimensional (2D) van der Waals (vdW) materials has garnered considerable attention in recent years. Strain engineering appears to be an effective way to manipulate magnetism in 2D materials, which was experimentally realized through, e.g., hydrostatic pressure for CrI_3 [1–3] and uniaxial strain for Fe_3GeTe_2 [4]. Theoretical calculations showed that uniform in-plane biaxial strain could tune the magnetic ground states of $CrSe_2$ and $CrTe_2$ monolayers, which is not yet verified experimentally [5]. In those studies, strain-induced lattice variations are either uniform (biaxial strain or hydrostatic pressure) or coupled with the Poisson's ratio of the material. Few previous studies [6,7] have dealt with in-plane strains being independently applied along the two lattice vectors of a 2D magnet, which usually occurs in epitaxy growth of layered materials.

Epitaxy of heterostructures usually introduces lateral interfacial strains because of lattice mismatch, which is a long-lasting way to maintain in-plane strain to the adlayers and is thus termed epitaxy strain [8–10]. vdW epitaxy refers to growth of 2D layers through vdW interactions on a dangling-bond-free substrate [11,12]. Magnetic 2D layers in vdW heterostructures show a strong ability to endure large lattice mismatches and thus significant in-plane strains [13–15]. A recent illustration of this ability is the epitaxy of monolayer $CrTe_2$ on graphene, where 7% compressive and 4% tensile epitaxy strain were applied along the two lattice vectors in which zigzag antiferromagnetic (AFM) ordering was observed [14]. In another study, 6% epitaxy tensile strain was applied in both lattice directions of a $CrSe_2$ monolayer through epitaxy growth on WSe_2, where a weak ferromagnetic (FM) state was reported [15]. In comparison with the ABAB order predicted in the freestanding $CrSe_2$ monolayer [14], this implies a potential ability of epitaxy strain to tune in-plane magnetism of 2D magnets, which has not yet been fully investigated. In-plane magnetism aside, an interesting question subsequently arises as to whether in-plane strain could change interlayer spin-exchange couplings.

In this study, we comprehensively considered the roles of epitaxy strain in tuning intra- and interplane magnetic couplings in $CrSe_2$ and $CrTe_2$ mono- and bilayers using density functional theory calculations. The predicted magnetic phase diagram of the $CrSe_2$ ($CrTe_2$) monolayer shows that its intralayer magnetic ground state is tunable among FM and three AFM orders within 2.5% (4.5%) in-plane strain. This tunability is primarily realized by changing Cr–Se–Cr (Cr–Te–Cr) angles, and thus the strength and type of Se-(Te-)mediated superexchange interactions between adjacent Cr atoms. Moreover, the varying in-plane strain also affects interlayer Se–Se or Te–Te distances, changing the interlayer magnetism between FM and AFM in two different manners [16]. A monolayer $CrTe_2$/bilayer graphene heterostructure model, recently prepared in an epitaxy experiment [14], was used to verify the reliability and feasibility of the phase diagrams.

Both freestanding 1T-$CrSe_2$ and -$CrTe_2$ monolayers take a hexagonal crystal structure with the P-3m1 space group [Fig. 1(a) and 1(b)] in their paramagnetic states. A $2 \times 2\sqrt{3}$ rectangular supercell was used for considering four magnetic—i.e., FM [Fig. 1(c)], ABAB [Fig. 1(d)] and AABB [Fig. 1(e)] striped AFM (sAFM); and zigzag (ZZ) [Fig. 1(f)] AFM—configurations in our density functional theory

[*]These authors contributed equally to this work.
[†]wcphys@ruc.edu.cn
[‡]wji@ruc.edu.cn

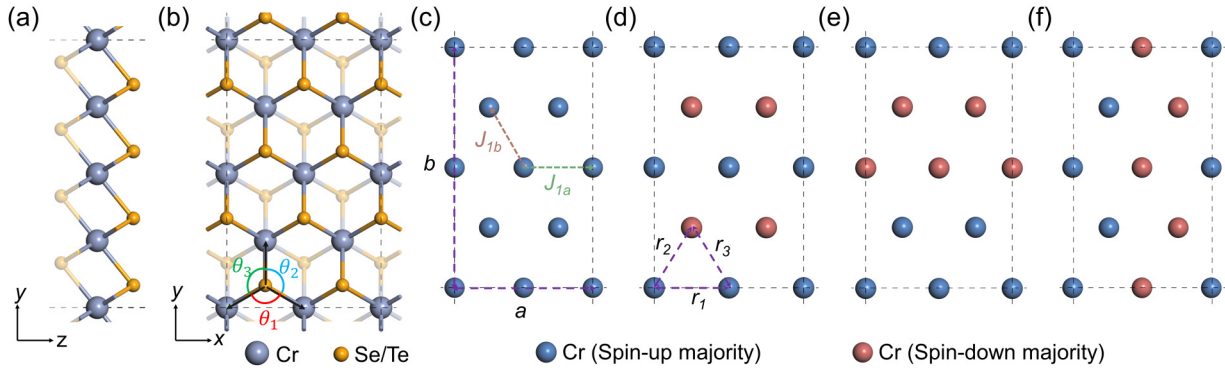

FIG. 1. Schematic models and magnetic configurations of monolayer $CrX_2 (X = Se, Te)$. (a) and (b) Side and top views of monolayer 1T-CrX_2. The orange and gray balls represent top-layer (solid) and bottom-layer (semitransparent) Se (Te) and Cr atoms, respectively. Three colored arcs denote three Cr–Se–Cr (Cr–Te–Cr) angles θ_1, θ_2, and θ_3, respectively. (c)–(f) Gray dashed rectangles label the $2 \times 2\sqrt{3}$ supercell used for considering four magnetic configurations. The dark-blue (red) balls indicate Cr atoms where spin-up (-down) is the majority spin component. Lattice constants a and b are labeled using the purple dashed lines in (c). Green and brown dashed arrows in (c) denote intralayer spin-exchange parameters J_{1a} and J_{1b} (nearly) in the a and b directions between the nearest Cr sites, respectively. Distances r_1, r_2, and r_3 in (d) represent the nearest Cr–Cr distances in three lattice directions.

calculations. Details of the calculations are documented in Supplemental Material Sec. "Computational Methods" [17] (see also Refs. [15,16,18–27] therein). Two ZZ-AFM configurations (ZZ1 and ZZ2) were observed and are compared in Supplemental Material Table S1 [17], which shows the superior stability of ZZ2 among all considered configurations of the $CrSe_2$ or $CrTe_2$ monolayer. The easy axes of $CrSe_2$ and $CrTe_2$ are both oriented in the yz plane and 110 ° off the z-axis (Supplemental Material Fig. S1 [17]). Here, we employ the $CrSe_2$ monolayer as a prototype for discussion while the results for $CrTe_2$ are documented in Supplemental Material Table S1 [17]. Its fully relaxed FM structure [Fig. 1(c)], shows the lattice constants $a = 6.84$ Å and $b = 11.84$ Å, the nearest Cr–Cr distance $r_1 = r_2 = r_3 = 3.42$ Å, and the corresponding Cr–Se–Cr angle $\theta_1 = \theta_2 = \theta_3 = 84.6°$, exhibiting a C_3 rotational symmetry, which was chosen to be the unstrained structure for further comparison.

However, the C_3 symmetry breaks in those AFM configurations. Introduction of AFM spin-exchange coupling (ABAB) shortens r_2 and r_3 to 3.32 Å, but elongates r_1 to 3.50 Å. The values of those angles split in accordance with the changes of Cr–Cr distances such that θ_2 and θ_3 decrease to 81.7 °, and θ_1 increases to 86.8 °. The lattice degeneracy further breaks in two ZZ configurations (see Supplemental Material Table S1 [17]). In the ZZ2 configuration, the two AFM coupled distances r_1 and r_3 split into 3.23 and 3.42 Å, respectively, while the FM coupled distance r_2 elongates to 3.47 Å. Associated angles change to $\theta_1 = 79.3°$, $\theta_2 = 84.4°$, and $\theta_3 = 85.9°$. These results indicate that magnetic configurations in the $CrSe_2$ ($CrTe_2$) monolayer are tightly coupled with their geometric structures, i.e., lattice constants, r_1 to r_3 and θ_1 to θ_3. Therefore, the influence of geometric structures on magnetic orders in both monolayers deserve a closer examination.

Figure 2(a) plots a magnetic phase diagram of the $CrSe_2$ monolayer as a function of lattice constants a and b. Tensile and compressive strains up to 8% were applied to the fully relaxed FM structure, i.e., $a = 6.84$ Å and $b = 11.84$ Å. While the FM configuration is favored with expanded lattice constants, compression in the a (b) direction changes the ground state to the ZZ (ABAB) configuration. The AABB state appears to be the most stable in a very narrow window between the FM and ABAB phases. The phase diagram of $CrTe_2$ [Fig. 2(b)] shows a similar feature, but with a more pronounced AABB region.

In the $CrSe_2$ ($CrTe_2$) monolayer, Se- (Te-)meditated Cr–Cr superexchange interactions dominate its intralayer magnetism, which is highly dependent on the Cr–Se(Te)–Cr angle [28]. Therefore, we defined spin-exchange parameters J_{1a} and J_{1b} along the two lattice directions [Fig. 1(b)] to explore the roles of varying in-plane epitaxy strain in changing θ_1 [Fig. 2(c)], θ_2 [Fig. 2(e)], J_{1a} [Fig. 2(d)], and J_{1b} [Fig. 2(f)] in the $CrSe_2$ monolayer as a prototype. Lattice constant a directly affects angle θ_1 and spin-exchange parameter J_{1a}, and consequently the in-plane magnetic configuration. As shown in Fig. 2(c)–2(f), in the FM region, angles θ_1 and θ_2 are close to 90º, and J_{1a} and J_{1b} bear negative signs, which favors the Cr–Cr FM superexchange. Angle θ_1 is nearly independent of lattice parameter b and gradually decreases with shrinking a values, i.e., from 90º at $a = 7.30$ Å to 76º at $a = 6.29$ Å with fixed $b = 11.84$ Å [the strain-free constant b value; Fig. 2(c)], which discredits the Se-meditated Cr–Cr FM superexchange along the a direction. As a consequence, J_{1a} reverses its sign from negative to positive at, e.g., $a = 7.04$ Å (∼2.9% tensile strain) with fixed $b = 11.84$ Å, as marked by the purple dot in Fig. 2(d), suggesting an FM-to-AFM transition. The sign reversal is the primary origin of the FM-to-ZZ-AFM transition.

The FM-to-ABAB transition shares a similar mechanism as lattice constant b becomes shorter. The shortened b lattice, and thus the decreasing θ_2 angle [Fig. 2(e)], directly flips the sign of J_{1b} at, e.g., $b = 11.96$ Å (∼1.0% tensile strain) with $a = 6.84$ Å (the strain-free constant a value), as marked by the purple dot in Fig. 2(f), but has little effect on J_{1a} except with strongly compressed b values. The flipped sign leads J_{1b} to favor the AFM superexchange at smaller b values. Thus, the AFM coupling occurs in the b direction, showing the sAFM-ABAB ground state at the right bottom part of the diagram. Competition between the FM and AFM couplings

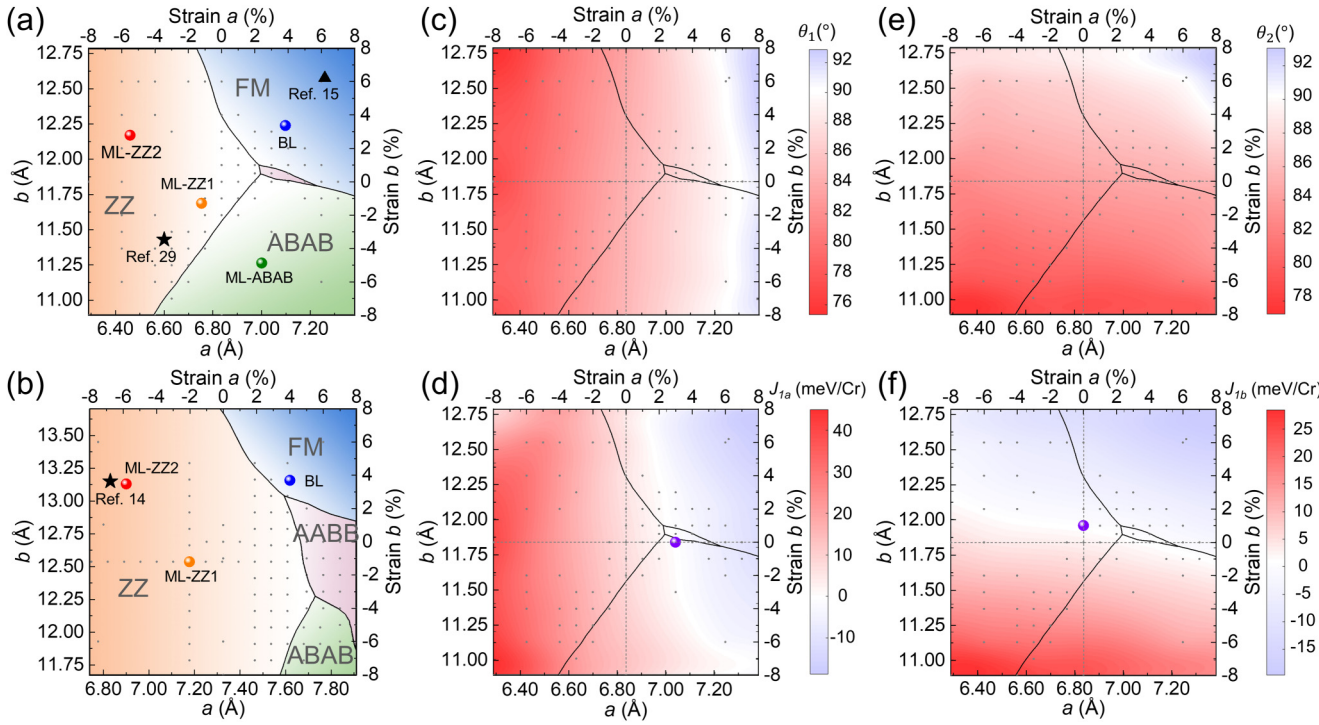

FIG. 2. Tunability of intralayer magnetism of monolayer $CrSe_2$ and $CrTe_2$. (a) and (b) Phase diagrams of monolayer $CrSe_2$ (a) and $CrTe_2$ (b) as a function of lattice constants a and b. Blue, orange, green, and purple components represent intralayer FM, ZZ, ABAB, and AABB, respectively. Each gray dot represents a theoretical data point to which the energies of those four configurations are compared. Red and blue (orange and green) balls label fully relaxed lattice constants under the most energetically favorable (metastable ZZ and ABAB; see Supplemental Material Table S1 [17] for more details) magnetic configurations in mono- and bilayer $CrX_2(X = \text{Se, Te})$, respectively. The black triangle and star mark the lattice constants of experimentally synthesized monolayer $CrX_2(X = \text{Se, Te})$ on different substrates. (c) and (e) Variation of θ_1 and θ_2 with the lattice constants in monolayer $CrSe_2$. (d) and (f) Mapping of exchange parameters J_{1a} and J_{1b} as a function of lattice constants. Positive (red) and negative (blue) areas represent AFM and FM spin-exchange coupling, respectively. Phase boundaries of monolayer $CrSe_2$ are labeled by black lines in (c)–(f).

along b results in an FM-sAFM transition configuration, i.e., sAFM-AABB, appearing in a very small region between FM and sAFM-ABAB, in which the two types of magnetic superexchange occur alternately. In terms of the boundary between ZZ-AFM and sAFM-ABAB, they show competing magnetic couplings in either J_{1a} (AFM vs. FM) and J_{1b} (FM vs. AFM). Thus, they roughly bisect the phase diagram outside the FM region. The magnetic ordering temperature is also largely affected by the in-plane strain owing to varied spin-change coupling and magnetic anisotropy energy, as discussed in detail in Supplemental Material Fig. S2 and Table S2 [17].

The phase diagram of monolayer $CrTe_2$ [Fig. 2(b)] shows a qualitatively similar but quantitatively different pattern to that of the $CrSe_2$ monolayer. Moreover, while it is comprised of those four phases, the ZZ-AFM phase occupies a larger region and the sAFM-AABB phase is more pronounced. A larger tensile strain of ~6.5% along the a direction ($a = 7.80$ Å at strain-free lattice constant $b = 12.69$ Å) is needed to trigger the positive-to-negative transition of J_{1a} (Supplemental Material Fig. S3 [17]), while that for J_{1b} of ~1.0% along the b direction ($b = 12.81$ Å at strain-free lattice constant $a = 7.33$ Å) remains comparable with the value for $CrSe_2$. Here, the robustness of the phase diagrams was verified by extensive testing and discussion of U dependencies (Supplemental Material Table S3 and Fig. S4 [17]) and functional dependencies (Supplemental Material Tables S4 and S5 [17]), which are also shared with the comparable transition strain previously revealed [5] using different functionals and U-J values (Supplemental Material Fig. S5 [17]).

Recently synthesized 2D $CrSe_2$ and $CrTe_2$ layers on various substrates, and their magnetic characterizations [14,15,29] confirmed the dependence of magnetic orders on lattice constants. In a $CrSe_2$ monolayer grown on WSe_2 [15], its lattice constant of 3.63 Å [$a = 7.26$ Å and $b = 12.57$ Å, black triangle in Fig. 2(a)] sits in the FM region of our phase diagram, consistent with the weak FM behavior found in Ref. [15]. A smaller lattice constant of 3.3 Å, corresponding to $a = 6.6$ Å and $b = 11.4$ Å [black star in Fig. 2(a)], was reported in another $CrSe_2$ monolayer grown on highly oriented pyrolytic graphite. Its lattice constants reside in the ZZ-AFM region, and thus is responsible for the absence of ferromagnetic signals in x-ray magnetic circular dichroism measurements [29]. In terms of $CrTe_2$ monolayers, a sample prepared on a SiC-supporting bilayer graphene substrate shows lattice constants $a = 6.8$ Å and $b = 12.15$ Å [black star in Fig. 2(b)], located in the ZZ region of the phase diagram, which was proved using spin-polarized scanning tunneling microscopy measurements [14].

Interlayer magnetic coupling introduces additional complexity of magnetism in $CrX_2(X = \text{Se, Te})$ bilayers. Tunability of intralayer magnetism aside, it would be a more interesting and yet-to-be-answered question as to whether

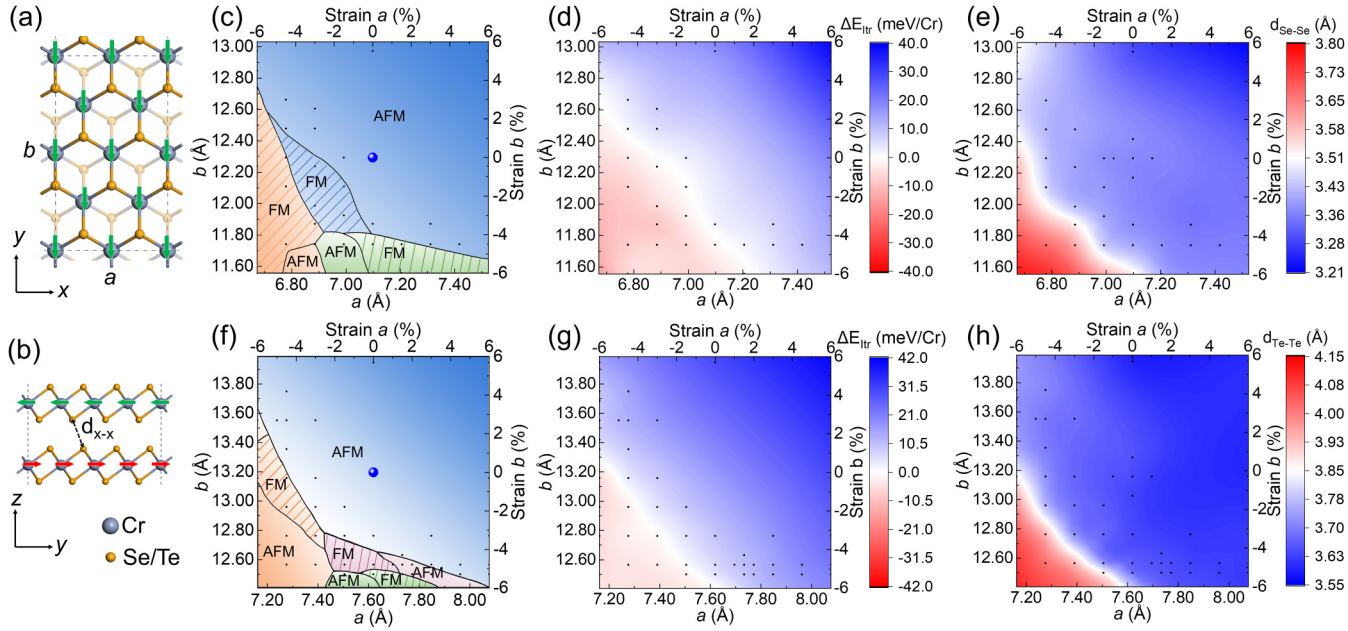

FIG. 3. Intra- and interlayer magnetisms of $CrSe_2$ and $CrTe_2$ bilayers. (a) and (b) Top and side views and magnetic ground state of an AA stacked CrX_2 bilayer. Gray and orange balls represent Cr and Se (Te) atoms, respectively. Lattice constants a and b are denoted in (a). Interlayer Se–Se (Te–Te) distance is labeled by the black dashed arrows in (b). Colored solid arrows on Cr represent the majority spin of up (red) and down (green). (c) Phase diagram of the $CrSe_2$ bilayer as a function of lattice constants a and b. While the color scheme and presentation style of data points are as the same as that used for the diagrams of monolayers, the shadowed and plain colored regions indicate interlayer magnetic couplings are FM and AFM, respectively. View (d) plots the energy difference between interlayer FM and AFM states of the intralayer FM configuration at different lattice constants. The blue (positive) region represents the favored interlayer AFM state, and the red (negative) region indicates the FM state. (e) Map of the interlayer Se–Se distance with respect to different lattice constants a and b. Panels (f)–(h) are duplicate panels (c)–(e) for the $CrTe_2$ bilayer case.

in-plane strain could tune interlayer magnetism in CrX_2 bilayers or few layers [Fig. 3(a) and 3(b)]. In other words, we are interested if the varying in-plane lattice constants change out-of-plane magnetic coupling in CrX_2 bilayers, which is discussed in detail as follows.

Figure 3(c) shows the phase diagram for the magnetic ground state of the $CrSe_2$ bilayer over in-plane lattice constants a and b. It is qualitatively comparable with that of the $CrSe_2$ monolayer in terms of intralayer magnetism. Intralayer FM and interlayer AFM, [FM-AFM, $a = 7.10$ Å and $b = 12.29$ Å, see Fig. 3(a) and 3(b)] was used as the strain-free ground state and thus the reference to calculate exact strain values in the $CrSe_2$ bilayer (see Supplemental Material Fig. S6, Tables S6 and S7 [17] for more details). The easy axis in the bilayer rotates 60 ° toward the z-axis from that of the monolayer (Supplemental Material Fig. S7 [17]). In a stacked bilayer of CrX_2, the interlayer charge sharing leads to a Cr e_g-to-t_{2g} charge transfer. The induced mixing of Cr^{4+} and Cr^{3+} favors intralayer FM via a double-exchange mechanism [17]. Meanwhile, the charge sharing also enlarges the in-plane lattice constants, resulting in increased Cr–Se–Cr angles and thus the more preferred FM ground state.

The interlayer magnetism in the bi- and thicker layers shows varied tunability under in-plane strain. As shown in the phase diagram [Fig. 3(c)], each colored region (intralayer magnetism), splits into two subregions denoting interlayer FM (shadowed color) and AFM (plain color) configurations, respectively. The interlayer AFM-to-FM transition follows two rules, depending on the intralayer magnetism. The interlayer AFM is more favored with larger in-plane lattice constants in the case of the intralayer FM configuration. For example, the FM-AFM state of $CrSe_2$ undergoes an interlayer magnetic transition to the FM-FM state under a 2.8% compressive strain applied in the a direction. Here, we defined the energy difference between the FM-FM and FM-AFM states as $\Delta E_{\mathrm{Itr}} = E_{\mathrm{FM\text{-}FM}} - E_{\mathrm{FM\text{-}AFM}}$, and plotted its values for $CrSe_2$ in Fig. 3(d), where it shows strong in-plane strain dependence. The AFM interlayer exchange (positive ΔE_{Itr}) is gradually suppressed by applying compressive strain to either lattice. Here, we define the negative of ratio of the interlayer strain to the uniaxial in-plane strain as the interlayer Poisson's ratio (see Supplemental Material Fig. S8 [17] for more details). If a finite positive value of it is presented, the shrank in-plane lattice constants should enlarge interlayer distance d_{X-X} and thus favor the interlayer FM coupling, following the Bethe–Slater curve-like (BSC-like) behavior and the superorbital-mediated superexchange mechanism that we previously revealed in MX_2 bilayers [16].

Figure 3(e) shows that $d_{\mathrm{Se-Se}}$ could vary from 3.21 to 3.80 Å in the range of ±6% in-plane strain for the $CrSe_2$ bilayer, which crosses the critical distance of 3.45 Å [16] for the interlayer FM-to-AFM transition. The interlayer Poisson's ratio is 0.48 (0.46) under the uniaxial strain along the a (b) direction for the $CrSe_2$ bilayer (Supplemental Material Fig. S8 [17]). Such a significant response of the interlayer distance to the

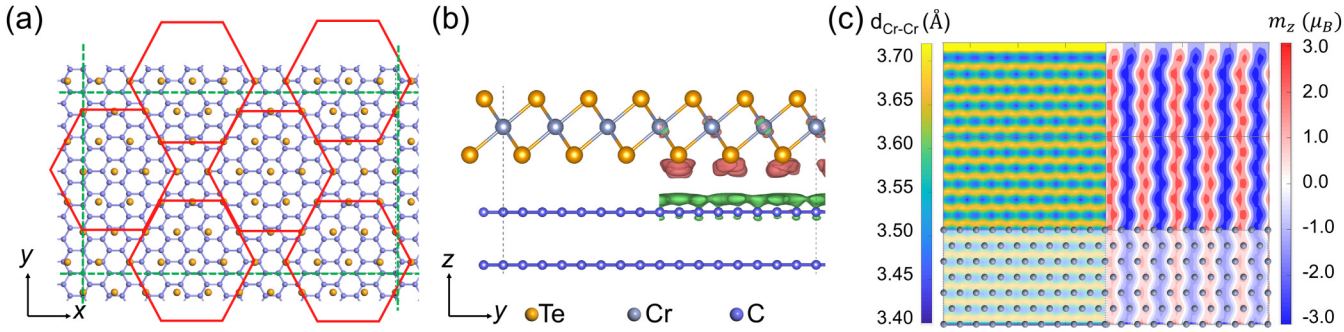

FIG. 4. Structure and magnetism of the epitaxial $CrTe_2$ monolayer on bilayer graphene (BLG). (a) Schematic model of a $10 \times 3\sqrt{3}$ $CrTe_2$/$16 \times 4\sqrt{3}$ BLG heterojunction. Only bottom-layer Te and top-layer C atoms are shown for clarity. (b) Side view of the interlayer differential charge density contour of the heterojunction with an isosurface level of 2.0×10^{-4} electrons/Bohr^3. Red and green contours represent charge accumulation and depletion, respectively. (c) Mapping of the nearest Cr–Cr distance (left panel) and magnetic moments (right panel) of Cr atoms in the heterojunction.

in-plane strain ensures the feasibility of tuning an out-of-plane interlayer magnetic configuration by applying in-plane stress fields. An opposite trend of interlayer magnetism and in-plane strain was found for the ZZ or ABAB intralayer magnetism in the $CrSe_2$ bilayer, termed reversed BSC-like behavior. This was ascribed to a competition between superorbital-mediated direct and super exchanges, which will be elucidated elsewhere.

The phase diagram of $CrTe_2$ bilayer [Fig. 3(f)] displays a comparable pattern to the $CrSe_2$ bilayer, except the missing FM-FM region and the additional intralayer AABB configuration. While the interlayer magnetisms of the intralayer ZZ-AFM and sAFM-ABAB configurations follow reversed BSC-like behavior, the interlayer spin-exchange interaction in the intralayer AABB configuration obeys BSC-like behavior, i.e., interlayer AFM (FM) for larger tensile (compressive or smaller tensile) strains. Another distinct difference of the $CrSe_2$ and $CrTe_2$ cases lies in the missing FM-FM region in the $CrTe_2$ diagram. The energy ΔE_{Itr} of the $CrTe_2$ bilayer [Fig. 3(g)] flips its sign in regions where the preferred in-plane magnetism already transforms into ZZ-AFM, sAFM-AABB, or sAFM-ABAB. Such delayed sign reversal is ascribed to a much larger transition distance of the $CrTe_2$ bilayer. Under the $\pm 6\%$ in-plane strain, interlayer distance d_{Te-Te} of the $CrTe_2$ bilayer varies from 3.55 to 4.15 Å [Fig. 3(h)] and the interlayer Poisson's ratio is around 0.61 (0.23) under the uniaxial strain along the a (b) direction (Supplemental Material Fig. S8 [17]). This distance range does not include the interlayer FM-to-AFM transition distance of 4.32 Å [16], but other in-plane magnetic configurations emerge before the interlayer AFM-to-FM transition occurs.

The phase diagrams imply that inter- and intralayer magnetic orders could be tuned by in-plane strain engineering, which usually utilizes slightly lattice-mismatched vdW substrates—namely, the epitaxy strain. We thus considered $CrTe_2$/bilayer graphene (BLG) as an example to model how in-plane epitaxy strain determines its magnetism. Figure 4(a) depicts a schematic model of a $10 \times 3\sqrt{3}$ $CrTe_2$/$16 \times 4\sqrt{3}$ BLG superlattice, as experimentally determined in a previous study [14]. While the graphene–$CrTe_2$ stacking order varies from site to site within a domain (red hexagons), no apparent charge transfer and interlayer wavefunction overlap [14–16,30] were observed between the $CrTe_2$ layer and the graphene substrate (see Fig. 4(b) and Supplemental Material Fig. S9 [17]). The in-plane epitaxy strain effect thus plays a dominant role in tuning the magnetism of the epitaxial layer. In this particular case, the nearest Cr–Cr distances are 3.42 and 3.70 ± 0.02 Å in the a and b directions [Fig. 4(c), left], respectively, which are within the ZZ region of the phase diagram and far from the phase boundaries [see black star in Fig. 2(b)], consistent with the robust ZZ-AFM state depicted in Fig. 4(c), right.

In summary, we revealed that in-plane epitaxy strain is capable of tuning both in-plane (intralayer) and out-of-plane (interlayer) magnetisms in epitaxial $CrSe_2$ and $CrTe_2$ mono- and bilayers. In terms of intralayer magnetism, the in-plane strain primarily changes the Cr–Se–Cr and Cr–Te–Cr angles that govern the intralayer spin-exchange couplings, giving rise to the ZZ, ABAB, and FM magnetic configurations. Our predicted phase diagrams of monolayers were confirmed with experimentally synthesized 2D $CrSe_2$ or $CrTe_2$ samples. A more striking effect is that the in-plane strain, through a finite Poisson's ratio, varies the interlayer distance, which subsequently determines the interlayer magnetism following a BSC-like or a reversed BSC-like behavior, depending on the in-plane magnetism. This exceptional effect enables tuning out-of-plane magnetism using an in-plane strain field. Upon epitaxy of those 2D magnets on a graphene substrate, epitaxy strain still dominantly determines their magnetism because of suppressed interlayer charge transfer. Our calculations suggest a considerable magnetoelastic effect in 2D $CrSe_2$ and $CrTe_2$, and indicate that their magnetisms can be manipulated in vdW epitaxy by in-plane strain from appropriately selected vdW substrates.

We thank Prof. Changsong Xu at Fudan University for valuable discussions. We gratefully acknowledge financial support from the Ministry of Science and Technology (MOST) of China (Grant No. 2018YFE0202700), the National Natural Science Foundation of China (Grants No. 61761166009, No. 11974422, and No. 12104504), and the Strategic Priority Research Program of the Chinese Academy of Sciences (Grant No. XDB30000000). C.W. was supported by the China Postdoctoral Science Foundation

(2021M693479). L.W. was supported by the Outstanding Innovative Talents Cultivation Funded Programs 2021 of Renmin University of China. Calculations were performed at the Physics Lab of High-Performance Computing of Renmin University of China, Shanghai Supercomputer Center.

[1] T. Li, S. Jiang, N. Sivadas, Z. Wang, Y. Xu, D. Weber, J. E. Goldberger, K. Watanabe, T. Taniguchi, C. J. Fennie, K. Fai Mak, and J. Shan, Pressure-controlled interlayer magnetism in atomically thin CrI_3, Nat. Mater. **18**, 1303 (2019).

[2] T. Song, Z. Fei, M. Yankowitz, Z. Lin, Q. Jiang, K. Hwangbo, Q. Zhang, B. Sun, T. Taniguchi, K. Watanabe, M. A. McGuire, D. Graf, T. Cao, J. H. Chu, D. H. Cobden, C. R. Dean, D. Xiao, and X. Xu, Switching 2D magnetic states via pressure tuning of layer stacking, Nat. Mater. **18**, 1298 (2019).

[3] Z. Lin, M. Lohmann, Z. A. Ali, C. Tang, J. Li, W. Xing, J. Zhong, S. Jia, W. Han, S. Coh, W. Beyermann, and J. Shi, Pressure-induced spin reorientation transition in layered ferromagnetic insulator Cr_2Ge_2Te, Phys. Rev. Materials **2**, 051004(R) (2018).

[4] Y. Wang, C. Wang, S. J. Liang, Z. Ma, K. Xu, X. Liu, L. Zhang, A. S. Admasu, S. W. Cheong, L. Wang, M. Chen, Z. Liu, B. Cheng, W. Ji, and F. Miao, Strain-sensitive magnetization reversal of a van der Waals magnet, Adv. Mater. **32**, 2004533 (2020).

[5] H. Y. Lv, W. J. Lu, D. F. Shao, Y. Liu, and Y. P. Sun, Strain-controlled switch between ferromagnetism and antiferromagnetism in 1T–CrX_2 (X = Se, Te) monolayers, Phys. Rev. B **92**, 214419 (2015).

[6] S. Yang, Y. Chen, and C. Jiang, Strain engineering of two-dimensional materials: Methods, properties, and applications, InfoMat **3**, 397 (2021).

[7] S. Zhang, R. Xu, N. Luo, and X. Zou, Two-dimensional magnetic materials: Structures, properties and external controls, Nanoscale **13**, 1398 (2021).

[8] B. A. Joyce, Molecular beam epitaxy, Rep. Prog. Phys. **48**, 1637 (1985).

[9] S. C. Jain, M. Willander, J. Narayan, and R. V. Overstraeten, III: Nitrides: Growth, characterization, and properties, J. Appl. Phys. **87**, 965 (2000).

[10] R. Ramesh and N. A. Spaldin, Multiferroics: Progress and prospects in thin films, Nat. Mater. **6**, 21 (2007).

[11] A. Koma, K. Sunouchi, and T. Miyajima, Summary Abstract: Fabrication of ultrathin heterostructures with van der Waals epitaxy, J. Vacuum Sci. Technol. B **3**, 724 (1985).

[12] A. Koma, Van der Waals epitaxy: A new epitaxial growth method for a highly lattice-mismatched system, Thin Solid Films **216**, 72 (1992).

[13] X. Zhang, Q. Lu, W. Liu, W. Niu, J. Sun, J. Cook, M. Vaninger, P. F. Miceli, D. J. Singh, S. W. Lian, T. R. Chang, X. He, J. Du, L. He, R. Zhang, G. Bian, and Y. Xu, Room-temperature intrinsic ferromagnetism in epitaxial CrTe2 ultrathin films, Nat. Commun. **12**, 2492 (2021).

[14] J. J. Xian, C. Wang, J. H. Nie, R. Li, M. Han, J. Lin, W. H. Zhang, Z. Y. Liu, Z. M. Zhang, M. P. Miao, Y. Yi, S. Wu, X. Chen, J. Han, Z. Xia, W. Ji, and Y. S. Fu, Spin mapping of intralayer antiferromagnetism and field-induced spin reorientation in monolayer $CrTe_2$, Nat. Commun. **13**, 257 (2022).

[15] B. Li *et al.*, Van der Waals epitaxial growth of air-stable $CrSe_2$ nanosheets with thickness-tunable magnetic order, Nat. Mater. **20**, 818 (2021).

[16] C. Wang, X. Zhou, L. Zhou, Y. Pan, Z.- Y. Lu, X. Wan, X. Wang, and W. Ji, Bethe–Slater-curve-like behavior and interlayer spin-exchange coupling mechanisms in two-dimensional magnetic bilayers, Phys. Rev. B **102**, 020402 (2020).

[17] See Supplemental Material at http://link.aps.org/supplemental/10.1103/PhysRevB.106.L081401 for the theoretical methods, geometric and magnetic details of mono- and bilayer $CrSe_2$ and $CrTe_2$, easy axis direction, strain effect on magnetic ordering temperatures, transferability of U-J values and functionals, mapping of Cr–Te–Cr angles and exchange parameters in monolayer $CrTe_2$, interlayer Poisson's ratio, and interlayer difference charge densities between monolayer $CrTe_2$ on mono- and bilayer graphene.

[18] P. E. Blöchl, Projector augmented-wave method, Phys. Rev. B **50**, 17953 (1994).

[19] G. Kresse and J. Furthmüller, Efficient iterative schemes for ab initio total-energy calculations using a plane-wave basis set, Phys. Rev. B **54**, 11169 (1996).

[20] M. Dion, H. Rydberg, E. Schröder, D. C. Langreth, and B. I. Lundqvist, Van Der Waals Density Functional for General Geometries, Phys. Rev. Lett. **92**, 246401 (2004).

[21] J. Klimeš, D. R. Bowler, and A. Michaelides, Van der Waals density functionals applied to solids, Phys. Rev. B **83**, 195131 (2011).

[22] J. Hong, Z. Hu, M. Probert, K. Li, D. Lv, X. Yang, L. Gu, N. Mao, Q. Feng, L. Xie, J. Zhang, D. Wu, Z. Zhang, C. Jin, W. Ji, X. Zhang, J. Yuan, and Z. Zhang, Exploring atomic defects in molybdenum disulphide monolayers, Nat. Commun. **6**, 6293 (2015).

[23] J. Qiao, Y. Pan, F. Yang, C. Wang, Y. Chai, and W. Ji, Few-layer tellurium: One-dimensional-like layered elementary semiconductor with striking physical properties, Sci. Bull. **63**, 159 (2018).

[24] Y. Zhao, J. Qiao, Z. Yu, P. Yu, K. Xu, S. P. Lau, W. Zhou, Z. Liu, X. Wang, W. Ji, and Y. Chai, High-electron-mobility and air-stable 2D layered $PtSe_2$ FETs, Adv. Mater. **29**, 1604230 (2017).

[25] J. P. Perdew, K. Burke, and M. Ernzerhof, Generalized Gradient Approximation Made Simple, Phys. Rev. Lett. **77**, 3865 (1996).

[26] M. Cococcioni and S. de Gironcoli, Linear response approach to the calculation of the effective interaction parameters in the LDA + U method, Phys. Rev. B **71**, 035105 (2005).

[27] J. Heyd, G. E. Scuseria, and M. Ernzerhof, Hybrid functionals based on a screened Coulomb potential, J. Chem. Phys. **118**, 8207 (2003).

[28] W. Geertsma and D. Khomskii, Influence of side groups on 90 degrees superexchange: A modification of the

Goodenough-Kanamori-Anderson rules, Phys. Rev. B Condens. Matter **54**, 3011 (1996).

[29] M. Liu, Y. L. Huang, J. Gou, Q. Liang, R. Chua, S. Duan Arramel, L. Zhang, L. Cai, X. Yu, D. Zhong, W. Zhang, and A. T. S. Wee, Diverse structures and magnetic properties in nonlayered monolayer chromium selenide, J. Phys. Chem. Lett. **12**, 7752 (2021).

[30] C. Wang, X. Zhou, Y. Pan, J. Qiao, X. Kong, C.-C. Kaun, and W. Ji, Layer and doping tunable ferromagnetic order in two-dimensional CrS_2 layers, Phys. Rev. B **97**, 245409 (2018).